Glioblastoma disrupts cortical network activity at multiple spatial and temporal scales

Jochen Meyer[1], Kwanha Yu[2], Ben Deneen[2,3,5], Jeff Noebels[1,3,4]

[1]Department of Neurology, Baylor College of Medicine, Houston, TX, USA; [2]Center for Cell and Gene Therapy, Baylor College of Medicine, Houston, TX, USA; [3]Department of Neuroscience, Baylor College of Medicine, Houston, TX, USA; [4]Department of Human and Molecular Genetics, Baylor College of Medicine, Houston, TX, USA; [5]Department of Neurosurgery, Baylor College of Medicine, Houston, TX, USA

Abstract

The emergence of glioblastoma in cortical tissue is accompanied by signs of neural hyperexcitability that may manifest with symptoms ranging from mild cognitive impairment to convulsive seizures. Glioblastoma exploits the complex interplay between neurons and glia to create a microenvironment favorable for its own expansion, impeding efforts to achieve long-term clinical remission compared to other solid tumors. We employed a novel CRISPR-Cas9 in-utero electroporation system to induce two distinct GBM tumor models in immunocompetent mice in combination with prolonged EEG recording and single and 2-photon imaging of calcium and glutamate reporters to analyze dynamic changes in peritumoral cortical network activity at different spatial and temporal scales. We find a biphasic elevation in neuronal calcium activity followed by a linear but only partially overlapping accumulation of peritumoral glutamate during tumor growth indicating these processes are not entirely coordinated. The patterns are strongly influenced by tumor genetics. The global changes in excitability homeostasis alter the higher order modularity and connectivity patterns of local and remote neuronal populations and can transform inter-areal brain information processing over time.

Introduction

Glioblastoma (GBM) is the most aggressive form of brain cancer that exploits its unique peritumoral cellular milieu in multiple ways to accelerate proliferation and invasion. At the leading edge, a hypersynaptic microenvironment (Lin et al., 2017) and early loss and impairment of interneurons (Hatcher et al., 2020; Tewari et al., 2018) promote a complex sequence of molecular and cellular remodeling leading to tumor-related epilepsy (TRE),

substantially reducing quality of life despite tumor resection (Cucchiara et al., 2020; Samudra et al., 2019). Only 40-60% of GBM cases present with seizures (Vecht et al., 2014). Distinguishing between healthy and epileptic tissue during tumor resection, as well as defining whether cortical network hyperexcitability in areas more distant than 0.5 mm from the tumor margin are recruited and how this remodeling can be suppressed to regain healthy cortical function remain major treatment challenges.

Recent work has demonstrated that GBM and TRE are intimately interconnected (Montgomery et al., 2020; Venkataramani et al., 2022; Venkatesh et al., 2019). GBM has been shown to preferentially dysregulate inhibitory interneurons (Campbell et al., 2015), upregulate expression of glutamate exporters (de Groot & Sontheimer, 2011; Takano et al., 2001), activate microglia (Hatcher et al., 2020), and modify synaptogenesis (Lin et al., 2017; Venkatesh et al., 2019) in a tumor driver gene-specific manner (Yu et al., 2020). Reports of GBM-induced changes in neurovascular coupling and neural activity dysregulation using human glioma cells implanted in mouse cortex offer additional evidence that improved understanding of this malignant progression may enable novel therapeutic opportunities (Gill et al., 2022; Montgomery et al., 2020; Tantillo et al., 2020; Venkataramani et al., 2022). With each of these advances in defining downstream molecular and cellular defects, the complexity of GBM biology and its interrelationship with surrounding excitable cortical tissue continues to grow. The heterogeneity of ambient pathophysiology driven by different tumor variants, the non-uniform landscape of malignant cell invasion, and the distinct stages of growth propelled by emerging waves of tumor cell clones require spatiotemporal dissection of tumor pathophysiology in order to improve our understanding of GBM progression.

We introduced a CRISPR-Cas9 guide RNA via intraventricular injection and IUE at E16 into immunocompetent mice to delete three human tumor suppressor genes *Pten*, *Nf1*, and *Trp53* and introduce a fluorescent protein label (designated the “Cr86” tumor model). We previously showed that this murine GBM causes a gradual increase of electrographic cortical hyperexcitability and seizures preceded by a reproducible pattern of peritumoral neuronal cell death, particularly in parvalbumin-positive (PV+) interneurons, degradation of perineuronal nets, widespread microglia activation, and waves of spreading depolarization providing a potential connection with this excitotoxicity (Hatcher et al., 2020; Radin & Tsirka, 2020). Peritumoral excess glutamate has long been identified as a candidate mechanism underlying GBM progression (de Groot & Sontheimer, 2011). Here, we used widefield and 2-photon serial cortical imaging of AAV-GCaMP7/8 or genetically expressed calcium indicators, as well as AAV-

iGlusnfr to monitor glutamate levels over time. Simultaneously recorded dual channel EEG, locomotion sensors, and cameras for limb, whisker and eye movements allowed us to characterize and control for the behavioral and attentional state of the animals during imaging. Our data reveal a nonlinear longitudinal sequence of changes in neuronal activity and functional connectivity at various spatial and temporal scales depending on the heterogeneity of the individual tumor morphology and invasiveness. We then repeated these measurements in animals that received CRISPR-constructs with additional expression of a recently identified tumor-associated variant (Glypican-6) implicated in promotion of synaptogenesis (Allen et al., 2012).

Methods

Animals: All animal procedures were carried out under an animal protocol approved by the Baylor College of Medicine IACUC. Mice were housed at 22 deg C under a 12h/12h/ on/off light cycle. Crispr mice were generated on CD-1 and C57BL/6 backgrounds as described (John Lin, 2017) and below. We used WT CD-1 mice for AAV-GCaMP, jrGeco1a, and iGlusnfr injections, or thy1-GCaMP6s-4.20 expressing mice on a mixed CD-1 x C57-BL6/J background.

In-utero electroporation (IUE) of CRISPR-Cas9 plasmid to generate glioma: In utero electroporations (IUEs) were performed on embryonic day 16 as described previously (Glasgow, SM et al. 2014). CRISPR- IUE GBM were generated by electroporating the three pX33- constructs targeting Pten, Trp53, and Nf1. Guide sequences for these CRISPRs were selected from previously published sequences (Xue, W. et al 2014, Chen, F. et al 2015) and validated in the IUE model. CRISPR-IUE GBM constructs were also electroporated with the pGLAST-PBase vector to visualize fluorescently labelled tumor cells.

EEG and headpost implant, virus injection, craniotomy: Mice were induced with 3-4% isoflurane in oxygen at 2 L/min flow rate until breathing slowed to ~60 bps. Full anesthesia was confirmed via tail pinch. Hair was removed by electric clippers (Wahl, Sterling, IL, USA), and residual hair removed using depilatory cream (Nair, Church & Dwight, Ewing, NJ, USA). The mouse was immobilized in a stereotactic frame with a gas-anesthesia adapter for neonatal rats and blunt-tip ear bars aimed at the upper mandible joint (Kopf instruments, Tujunga, CA, USA). The scalp was disinfected using 3 alternating applications of betadine scrub and 70% EtOH, and the animal was covered with a fenestrated sterile drape sparing only the disinfected scalp. All surgical instruments were autoclaved prior to use. Using pointed tip surgical scissors

(WPI, Sarasota, FL, USA), a ~1x1 cm square skin flap was removed to expose the skull bone. Using a no. 10 scalpel blade and serrated forceps, the periosteum was removed, and residual bleeding was absorbed with sterile cotton swabs. A thin layer of Vetbond cyanoacrylate (3M, Maplewood, MN, USA) was applied to close the scalp wound and ensure a dry edge of the remaining scalp skin to promote healing and avoid inflammation/infection or excessive scar tissue formation. Next, a custom-made EEG adapter with attached wires (2 recording channels, one reference, each made from Teflon-coated silver (WPI, Sarasota, FL, USA) wire with ~0.5mm tips exposed, beveled using 600 grit sandpaper and chlorided in NaCl) was attached using Krazy glue (Elmer's, Westerville, OH, USA) to the skull bone ~3 mm anterior of lambda. A dental drill with ¼ carbide burr tip (Midwestern, Henry Schein, Melville, NY, USA) was used to make 3 burr holes, one over the cerebellum (bregma -3 mm, 2.5 mm lateral), and two at lambda +1 mm, 5 mm lateral on both hemispheres, making sure not to break through the bone but to create small cracks exposing the underlying dura mater. The silver wire tips were carefully inserted just below the bone to touch the dura, and the holes were immediately sealed with a small drop of Vetbond. A mixture of dental cement powder (Lang dental, Wheeling, IL, USA) and charcoal powder (10:1) was mixed with dental cement fluid (Lang dental, Wheeling,IL, USA), and applied to the skull in a donut shape, approx. 5 mm high and creating a ~15 mm diameter well. The custom-designed aluminum head bar (emachineshop, Mahwah, NJ, USA) was gently pushed into the dental cement to sit flush with the skull. A small amount of Vetbond was added to the inside walls of the headpost to promote permanent attachment. After the dental cement cured, excess cement was removed using the dental drill. A nanoliter injector (Nanoject II, Drummond scientific, Broomall, USA), was used to inject AAV solutions. Glass pipettes were pulled using a Sutter P-87 horizontal pipette puller (Sutter instruments, Novato, CA, USA) and tips were broken on the filament of a vertical puller (Narishige, Japan) to create a sharp, ~10-20 µm wide opening. The pipette was backfilled with corn oil, and ~5 µL virus solution was aspirated from a sterile piece of parafilm using the Nanoject II. Depending on the experimental paradigm, we used one of the following (combinations of) AAV's:

pGP-AAV-syn-jGCaMP7f-WPRE (Addgene, Watertown, USA), diluted 1:2.5 in sterile Cortex buffer (CB),

or AAV-FLEX-GCaMP8m + AAV-CamKIIa-0.4-Cre, diluted 1:1.5 in sterile CB

or AAV-jrGeco1a, diluted 1:3 with sterile CB,

or AAV-FLEX-iGlusnfr-184 + AAV-Ef1α-Cre, diluted 1:1.5 in sterile CB,

or AAV-FLEX-iGlusnfr-184 + AAV-CamKIIa-0.4-Cre, diluted 1:1.5 in sterile CB.

A total of 8 or 6 (depending on the unobstructed skull area available) equidistant injection locations were selected with the goal to maximize coverage of sensory and posterior motor cortex. For each hemisphere, these were at [bregma –3.5 mm; 2.5 mm lateral], [bregma –2 mm; 1 mm lateral], [bregma –2 mm; 4 mm lateral], and [bregma –0.5 mm; 2.5 mm lateral]. At each location, a total of 400 nL AAV-solution at 2 depths, ~300 µm, ~600 µm, were injected into the cortex in 9.2 nL/pulse increments separated by 10s. After the last pulse in each location, the pipette remained in place for 5 min to minimize backflow and promote virus diffusion. The Nanoject was mounted at a 25-degree angle relative to the skull surface at each location and actuated by a manual and 1-direction motorized micromanipulator (WPI, Sarasota, FL, USA) at speeds of ~600 µm per min. After the last injection, the skull was covered with Vetbond and dental cement. Mice were allowed to recover for ~10 days post injection with meloxicam analgesic administered for the first 3 days. For the second surgery, induction and stereotactic positioning were performed as described above. The dental cement covering the skull was removed. A single-pane #1 cover glass (22x11 mm, Thomas Scientific, Swedesboro, NJ) was cut and adjusted to the individual dimensions (approx. 7.5x6 mm) of the exposed skull bone by scoring the glass with a sharp-tip drill bit. The cover glass was then submerged in 70% EtOH for >10 min. The outline of the cut glass was transferred and a corresponding groove carefully drilled while cooling the bone every 10-20s with compressed air and stopping short of the dura to avoid damage. A thin strip of bone covering the superior sagittal sinus was thinned but not removed. Before carefully removing the bone, it was soaked to soften for 5 min with sterile CB. Any superficial bleeding was controlled with small pieces of sterile surgifoam (Ethicon, Cincinnati, OH, USA), previously soaked in sterile CB. The dura was carefully removed by grasping, stretching and gently piercing it with a 30G needle, then peeling it off with serrated forceps. The cover glass was carefully placed and initially attached with Vetbond while gently applying downward pressure, ensuring that any gaps between the bone and the glass were filled with Vetbond without reaching the brain. After polymerization of the Vetbond, a few drops of cyanoacrylate glue were added to secure the glass in place, and finally a thin layer of dental cement around the edge of the glass was applied to seal it in place. Typically, this preparation allowed for >6 weeks of cellular resolution 2-p imaging and >10 weeks widefield 1-p imaging. If redness or signs of inflammation was seen, dexamethasone (0.5 mg/kg) was given for 3 days.

In vivo 2-photon and 1-p widefield imaging: Mice were typically imaged every 4-6 days starting between P45 and P55, and every 1-3 days once spontaneous seizures were

detected until the animal appeared moribund and was euthanized with CO_2. The mouse was headfixed and allowed to freely run on top of a custom-built Styrofoam wheel (12 cm diameter), whose rotational speed was recorded by a velocity sensor. Both imaging modalities are integrated in a Prairie Ultima IV (Bruker, Billerica, MA, USA) modified in vivo 2-photon microscope. One-photon image sequences were acquired with a pco.Edge 4.2 sCMOS camera (pco, Germany), mounted on top of the scan head of the Bruker Ultima IV microscope with a 2x objective lens (CFI Plan Apo Lambda 2X, Nikon, Melville, USA), yielding a raw (unbinned) resolution of 3.62 µm/pixel (FOV = 2060x2048 pixels). Widefield movies were acquired using 2x or 4x software binning at 100Hz (10ms exposure duration). Blue illumination light (for GCaMP indicators or GFP expressed in tumors) was generated by a Xenon arc lamp (Zeiss, Germany), guided through a 480/20 excitation filter. For tagBFP labeled tumors, a 400/40 excitation and 480/40 emission filter was used. For GCaMP emission and jrGeco1a or RFP excitation, a 525/70 filter was used, and for jrGeco1a and RFP emission, a 620/60 filter was used. For iGlusnfr (Venus) imaging, a 517/20 excitation and 554/23 emission filter set was used. Images were acquired at 100 Hz with 2x2 or 4x4 digital binning (1020x1024 or 500x512 pixel FOV, respectively) on a Lenovo P920 workstation (Lenovo, Morrisville, USA). EEG signals were amplified (HP 0.1 Hz, LP 5 kHz, gain x100) using a Model 1700 differential AC amplifier (A-M systems, Sequim, USA), digitized with a USB-6211 multifunction I/O device (National Instruments, Austin, USA) and recorded using WinEDR freeware (Strathclyde University, United Kingdom) at 10 kHz. Pupil size of the right eye was illuminated with an IR LED and recorded at 30 Hz with a GC660 IR camera (Allied Vision Technologies, Newburyport, USA) using custom Matlab routines (Mathworks, Natick, USA). The position and movement of the animal's head, whiskers, front paws and frontal parts of the body was monitored and recorded at 30 Hz with another IR camera, triggered by the WinEDR output signal generator (model SC1280G12N, Thorlabs, Austin, USA). These recordings were used to detect and exclude periods containing movement artifact that might contaminate the pixel by pixel analysis of imaging data.

2-photon images of calcium and glutamate reporter activity were acquired with a Prairie Ultima IV 2-photon microscope using a ×25 objective, 1.1 NA, or a ×16 objective, 0.8 NA, at 920 nm (GCaMP7/8) or 1000 nm (jrGeco1a) under spiral (10–20 Hz frame rate) or resonant scan mode (30-35 Hz). We used a 525/70 nm emission filter for GCaMP6/7/8 indicators, a 554/23 nm filter for iGlusnfr, and a 620/60 nm filter for jrGeco1a emission. We targeted primarily L2/3 (mean depth below pia: 163 µm, range 100–240 µm). We also imaged some FOVs in L4 (mean depth below pia: 383 µm, range 360–395 µm), and several FOVs in L5 (mean depth below pia: 570 µm, range 510–640 µm). Laser output power under the objective was kept below 50 mW,

corresponding to ~20% of power levels shown to induce lasting histological damage in awake mice (Podgorski & Ranganathan, 2016). Mice were imaged while awake, head-posted in a holding frame and allowed to run freely on a circular treadmill.

1-photon image preprocessing: Widefield images were processed using a custom-written Matlab pipeline partially based on previously published analysis methods [suite2p/caiman/seqnmf/mesoscale brain explorer/ofamm toolboxes]. Briefly, recordings were saved by the pco acquisiton software as multiple 2GB tiff stacks. These were loaded into MATLAB, downsampled to a spatial resolution of ~36 μm/pix, motion-corrected ([normcorre-function], Matlab (Pnevmatikakis & Giovannucci, 2017)), multiplied by a mask tiff file to suppress any artifactual signals from the vasculature (manually constructed in imageJ), and converted into DF/F movies, saved as a single .h5 file. Next, the FOV was divided into 500x500 μm square ROIs, and for each of the ROIs a DF/F trace over time was computed and detrended. In addition, the movies were temporally downsampled to 3 Hz and a modified version of a previously published CNMF algorithm for unbiased detection of neuronal signals over time was used to find natively clustered ROIs corresponding to independent activity patterns (parameters used for this algorithm: min size = 0.008 mm^2 (corresponding to a 50 μm radius), max size = 10 mm^2). Thus, we constructed two separate sets of activity traces, one purely based on equally spaced coordinate windows within the FOV, the other based on CNMF significance measures. The other acquired voltage traces corresponding to wheel motion, visual stimulus, IR camera trigger, and EEGs were then downsampled and aligned to the DF/F traces.

Snapshots (average of 20 frames) of baseline activity during quiet wakefulness were taken at full resolution (2048x2048 pix) and 100 ms exposure time. To extract the rate of change in fluorescence for both calcium, glutamate and tumor indicators, we first scaled all images from each animal equally, then calculated the ratio of images taken at consecutive recordings, divided by the number of days between the sessions, and normalized by the mean intensity of all pixels of the resulting ratio image (see figures 2, 3).

Analysis of widefield calcium signal in relation to tumor growth. Detrended and normalized DF/F image sequences were spatially downsampled by a factor of 8, resulting in a final resolution of ~240 microns per pixel. Active running and whisking episodes were computed and excluded to select images corresponding to 300 sec of quiet wakefulness for each recording. For each pixel, a DF/F trace was extracted, and calcium events were identified using a thresholding algorithm, taking into account variations in the baseline noise level for each pixel. From here, we defined the following metrics that provide information about different aspects of

the calcium activity patterns observed: 1) “activity per min”: the mean of the DF/F trace computed over the 300 sec trace. 2) “events per sec”: the rate of identified calcium transients after thresholding at 3SD above the median, divided by 300 sec. 3) “mean amplitude”: the maximum DF/F value of each calcium event averaged over all identified events per pixel. This corresponds to a measure of the maximal firing rate achieved during a single calcium transient 4) “mean area”: The area under each event, averaged over the 300 sec trace for each pixel. This corresponds to a relative measure of sustained or “integrated” firing rate during the duration of a calcium transient. Note that this measure does not distinguish between a long, low-amplitude event and a short, high-amplitude event of the same area under the curve. 5) “rhythmicity”: This metric was computed by generating a distribution of all inter-event intervals, and calculating the inverse of its standard deviation divided by the mean. Note that this metric shows the regularity of calcium events, but does not contain information about the frequency at which they occur. Changes in these metrics for all FOV pixels pooled together, over time, were quantified using a non-parametric ANOVA equivalent (Kruskal-Wallis test) across recordings. For each recording session, a reference image of the tumor (using either a green/red filter for RFP, blue/green for GFP, or 400 nm/blue for BFP) was acquired, spatially downsampled and aligned with the calcium signal image to obtain a pixel mask of the tumor mass location. Tumor growth rate for each period between recording sessions was calculated by dividing the difference in tumor fluorescence between consecutive recordings by the number of days in between. Next, the distance of each pixel from the closest tumor pixel was calculated. A linear regression between all tumor distances and the 5 metric values was performed and adjusted R-square as a goodness-of-fit parameter calculated. The tumor distances were circularly shuffled 500,000 times, and the regression was performed for these bootstrapped repetitions. Significance (p-value) was then computed as the fraction of bootstrapped trials with a higher R-square than the actual value. Significance was quantified as a function of tumor growth rate. For recordings with significant changes, FOV pixels were then divided into distance bands at 0.75-mm steps from the tumor. Metric distributions for each bin were compared with a Kruskal-Wallis test, and distance-related changes were depicted as boxplots showing the defining features of the metric distributions in each band.

Results

Chronic monitoring of cortical excitability changes during GBM progression

An experimental schema of the project is shown in Figure 1. We induced gliomas by electroporating a CRISPR-Cas9 sgRNA targeting Pten, Nf3, and Tp53 in the ventricles of E16.5 murine embryos (Fig. 1a). Depending on the color of the fluorescent calcium or glutamate indicator used in the imaging of each cohort, a red (RFP), green (GFP) or blue (tagBFP) fluorescent protein is encoded in the CRISPR construct. At P32-35, fluorescent activity indicator AAVs were injected intracortically under anesthesia (AAV-GCaMP7f, AAV-jrGeco1a, AAV-FLEX –GCaMP8m + AAV-CamkIIa-0.4- Cre or AAV-FLEX-iGlusnfr + AAV-Ef1α-Cre or AAV-CamkIIa-0.4-Cre, 6-8 overlapping injections of 200 nL each at 2 depths). For thy1-GCaMP6s line mice, no AAV injections were performed. AAV expression was consistently widespread and uniform after 2 weeks. Replacing a ~7x5 mm rectangular part of the dorsal skull surface with a cover glass and implanting 2 epidural EEG leads allowed us to image both widefield and cellular resolution neural activity using an integrated microscope system with additional sensors and cameras for continuous tracking of the animals' behavioral status (Fig. 1b). An example of the acquired activity traces is shown in Fig 1c. Cranial windows typically remained optically clear for up to 18 weeks, allowing 1- and 2- photon imaging as shown in Fig 1d (P62 – P189). We were able to image calcium and glutamate indicators simultaneously in conjunction with the fluorescent tumor markers and separate their signals using appropriate color filters.

We simultaneously imaged both brain hemispheres through chronic cranial windows exposing the majority of dorsal sensory and posterior motor cortices during tumor progression to follow glioma invasion and changes in peritumoral neural activity patterns over 6-18 weeks per animal. Figure 2 shows images of two different animals, one expressing a calcium indicator (thy1-GCaMP6-s, magenta, (2A), the other expressing a glutamate indicator (AAV-FLEX-iGlusnfr + AAV-Ef1α-Cre, orange, 2B). These are representative examples showing the minimal impact of the invading tumor on baseline neuronal calcium signaling distant from the tumor over a 5-week period. The baseline calcium activity grows between P63 and P78, followed by a flattening of the rate of change over subsequent weeks until death of the animal. In contrast, Fig 2B shows that the glutamate signal, both peritumoral and remote, grows steadily and significantly over the same time period, engulfing both tumor rich and tumor poor regions alike, however with considerable discordance with the tumor margins. Large glutamate rich areas are concentrated in some but not all tumor-bearing cortex.

Fig 2C-D assess these interim changes at a finer time scale. The magnitude of progressive change in neuronal activity and glutamate levels during these intervals can be quantitatively resolved.

We quantified the evolution of baseline peritumoral neuronal calcium signaling and glutamate intensity in mice at a sampling time scale ranging from 3-7 days over a period of 6-11 weeks (n=8 mice with calcium indicator, n=7 mice with glutamate indicator) determined by survival. In Fig 2C, the B/W panels taken from an exemplary animal show the baseline calcium signal snapshots. To assess regional changes at sequential time intervals, we calculated the coefficient of variation for each pixel between consecutive imaging time points as the pixel-wise ratio of the images from two consecutive time points, divided by the number of days between recordings and the mean brightness of all pixels. The resulting colorized panels (right) show a relative increase in calcium in red and a decrease in blue (white = no change) between days P56 and P99. In Fig 2C, the rapid and spatially heterogenous elevation of calcium activity takes place early, during the period P56-P69, followed by an indolent period with little further change in overall baseline calcium activation (shown in white).

In contrast, similar analysis using an equalized brightness scale in Fig 2D shows a steadily accumulating glutamate signal between P59 and P93. The landscape of glutamate accumulation is largely but not entirely peritumoral. At early stages, in some animals, it begins to accumulate before the apparent arrival of dense cortical tumor signal (D, P59-P63), then intensifies over and extends far beyond the labeled tumor margin, while at later stages it engulfs the entire tumor. Also striking is the continued dynamic instability of glutamate levels throughout the growth period (regions of red and blue in colored images below).

These profiles varied somewhat in each animal (Fig 2E). To summarize the overall progression, we binned the recordings into time intervals of 10 days between P45 and P135, and computed the 90th percentile of the resulting distributions for each bin to account for potential sampling bias towards more frequently sampled animals and potential outliers. Fig 2E-F) shows the resulting evolution of calcium (blue) and glutamate (orange). Coefficient of variation (CV) values over time for 8 and 7 animals, respectively. On average, the calcium CV was 56% lower than the glutamate CV (0.04 +/-0.0044 sem vs 0.09 +/- 002 sem, $p = 0.008$, Wilcoxon ranksum test).

Overall, the changes in calcium baseline fluorescence appeared consistently smaller than the changes in glutamate reporter brightness and showed distinct spatial profiles. This result demonstrates a significant and dynamic change in extracellular glutamate levels during

the progression of GBM invasion that in some nontumor regions correlates poorly with neuronal calcium activity levels. These nonlinear glutamate accumulations are not mirrored by changes in calcium baseline of comparable amplitude, and may precede intimate contact with tumor cells and extend several millimeters away from the tumor margin, even including large areas remote from the tumor in the contralateral hemisphere.

Different tumor driver variants generate distinct excitability dynamics

Next, we analyzed the spatiotemporal patterns of cortical glutamate activity during tumor invasion to compare the Cr86 tumor model with a second, faster growing model consisting of the same gene deletions plus an overexpression of glypican 6, (GPC6) an astrocytic promoter of synaptogenesis (Allen et al., 2012). First, we calculated the CV between recordings as described in the previous section. Example images from a Cr86 tumor animal computed from 8 imaging sessions between P59 and P125 are shown in Figure 3, using the same color scale as in Figure 2. In contrast with the large dynamic changes in tumor fluorescence in the Cr86 model (Fig 3A), the GPC6 animal (Fig 3B) exhibits significantly attenuated variations in tumor glutamate CV over time (images calculated from 10 time points between P62 and P140). We analyzed a total of 11 Cr86 and 8 GPC6 animals and found that the CV was on average 49% lower for GPC6 than for Cr86 tumors (0.032 +/-0.005 sem vs 0.065 +/- 0.011 sem, $p = 0.032$ Wilcoxon ranksum test, figure 3C, middle). Of note, the additional expression of GPC6 did not significantly change mean survival rates compared with the Cr86 animals, despite the differences in tumor cortical invasion dynamics, indicating that those two processes may be determined by independent mechanisms, for example, degree of subcortical extension of the tumor.

Analyzing the excitability profile relative to distance from tumor edge

Next, we set out to determine how mesoscale cortical activity patterns change, both as a function of distance from the tumor edge and time, as we record widefield calcium activity at different time points during tumor progression. Figure 4 summarizes the analysis steps taken from raw image data to the statistical analysis of activity patterns. First, each calcium image series was temporally and spatially downsampled. Running and whisking activity were quantified for the duration of the recording, and 300 seconds of images corresponding to quiet wakefulness were selected for further analysis to exclude movement and arousal related artifact (Fig 4a). Tumor spatial coordinates were extracted, and the distance between each pixel and the nearest part of the tumor edge was computed (Fig 4b). DF/F traces for each pixel were then processed to identify individual calcium events, and the following metrics were extracted: mean

event amplitude, mean event area, event rate per sec, event rhythmicity, and overall mean DF/F value (Fig 4c). To quantify the relationship between the calcium activity metrics and the distance to the tumor, the R-square value of a linear fit of all pixel values was computed. To ascertain statistical significance of the linear fits, we generated surrogate control distributions of R-square values derived from circularly shuffled distance values and the corresponding pixel metrics (500,000 repetitions, (Fig. 4d). In order to determine potential relationships between activity metrics and tumor distance without relying on linear regression, we combined pixels into tumor-equidistant bins of 0.75 mm width. This allowed us to compare the metrics both across distance bands for separate timepoints, and across timepoints for the separate distance bands using a nonparametric ANOVA (Kruskal-Wallis) test (Fig 4e).

Periods of rapid tumor growth acceleration are associated with elevated activity patterns near the tumor margin

Analyzing calcium activity on time scales of seconds to minutes across multiple stages of tumor invasion, we found that certain aspects, or metrics, of the DF/F calcium event structure significantly changed over time. We first made whole-FOV maps of the 5 calcium activity metrics introduced in Figure 4, and show examples from a Cr86 tumor animal (Fig 5a, colored FOV maps from P42 – P129) and a GPC6 tumor animal (Fig 5b, colored FOV maps from P62 – P134). We independently analyzed the changes in the 5 metrics for the whole FOV over time (averaged over all pixels; mean +/-sem across time are shown to the right hand side of the FOV plots), and as a function of distance from the tumor at each time point, analogous to Fig 4d. The distance band plots below the FOV metric plots and the curves underneath demonstrate that for certain metrics, there was a strong relationship between the reduction in activity with increasing tumor distance and the tumor growth rate, which exhibited a highly nonlinear profile in most animals such as the Cr86 one shown here. Calcium event amplitude, which can be thought of as the number of neurons in a local ensemble firing strongly together, was highly dependent on tumor distance for this Cr86 tumor, however this was not the case for the GPC6 example (Fig 5b). In Fig 5c (i), we show that across all recorded animals, the calcium activity metrics across the whole FOV (mean DF/F, amplitude, area, and events/sec shown here), normalized by the value of the first recording of each animal, did not depend on whether the tumor growth rate was low (<10e5 μm^2/day) or high (>10e5 μm^2/day). This was equally true for GPC6 tumors (ii). However, when examining the relationship between the dependence of calcium event amplitude and tumor distance as a function of tumor growth rate, we found a discrepancy between Cr86 and GPC6 tumors. Fig 5c (iii) shows that the difference between significance (p-values) derived

from the distance-based analysis of 32 recordings in 4 Cr86 animals calculated when tumor growth rate was low versus high was significant (Wilcoxon ranksum test, $p = 0.003$), whereas it was not for GPC6 tumors ($p=0.7$, 12 recordings, 2 animals). Therefore, whereas the growth rate of both tumors studied here did not affect the overall change of several calcium activity metrics we analyzed, we uncovered a significant relative hyperexcitation of tumor-adjacent cortex in Cr86 when tumor growth rates were high, which was not observed for GPC6 tumors.

Discussion

GBM has consistently ranked as one of the least successfully treatable malignancies with the highest recurrence and lowest survival rates for many decades, despite the introduction of several promising therapeutic interventions (Campanella et al., 2020) . In addition to poor survival prognoses, GBM routinely occurs with severe neurological comorbidities including seizures (Pace et al., 2013; Samudra et al., 2019), suggesting a functional interrelationship. In fact, several studies have recently indicated that anti-epileptic drugs (AED's) may slow tumor progression in addition to suppressing seizure activity (Cucchiara et al., 2020; Eckert et al., 2017; Gefroh-Grimes & Gidal, 2016; Kerrigan & Grant, 2011). A wide spectrum of possible underlying causes for GBM's ability to use neural hyperexcitation for to its own advantage and its resistance to therapy have been proposed (Jung et al., 2019; Keough & Monje, 2022; Torres & Canoll, 2019) . Recent studies provide multiple lines of evidence for the ability of GBM to promote its spread by taking advantage of the unique microenvironment in the brain that results in a complex feedback system of increased glutamate metabolism (Alcoreza et al., 2019; Buckingham et al., 2011; Sørensen et al., 2018), synaptogenesis (Venkataramani et al., 2019; Venkatesh et al., 2019; Yu et al., 2020), suppression of GABAergic inhibition (Campbell et al., 2015; Tewari et al., 2018), and alteration of other signaling pathways (Li et al., 2022; Piao et al., 2009; Venkatesh et al., 2015) .

Despite these advances, many questions about GBM progression and how the reciprocal feedback mechanisms with the surrounding neural activity unfold remain unanswered. We set out to measure these interactions in a recently established GBM model utilizing CRISPR/Cas9 gene editing in utero to induce native glioma growth in an immunocompetent host organism (Lin et al., 2017; Yu et al., 2020). This GBM model has been shown to recapitulate many hallmarks of the human disease and has revealed, among other phenomena, reduced inhibitory interneurons in the tumor margin, activated microglia populations, reduction in perineuronal nets, and upregulation of xCT-dependent astrocytic

glutamate export (Hatcher et al., 2020). However, neither the growth rate, borders, or zones of hyperexcitability are uniform or predictable, and defining the progression and extent of malignant cortical hyperexcitability in a growing tumor requires the ability to serially monitor neuronal network activity over prolonged periods in vivo during tumor cell invasion.

We combined two distinct genetically engineered models of glioma in immunocompetent mice with chronic in vivo imaging and EEG recordings to follow disease progression, specifically neuron-tumor interactions, in unprecedented spatial and temporal detail. On time scales of days to weeks, we show that glutamate accumulation, as measured by a genetically expressed fluorescent glutamate reporter (AAV-iGlusnfr), undergoes early dramatic spatial shifts as tumor cells invade the cortex, resulting in large regional changes both near and distant from the tumor margin. In contrast, baseline calcium fluorescence, corresponding to ongoing spontaneous synaptic and action potential activity in superficial cortex, changes less significantly at later stages. This result supports recent evidence of multiple molecular pathways used by GBM to alter the extracellular microenvironment in favor of its own growth by raising free glutamate levels (Buckingham et al., 2011; Sørensen et al., 2018; Takano et al., 2001; Ye & Sontheimer, 1999), apparently independently of adjacent tonic firing or synaptic activity levels. Note that changes in DF/F calcium patterns other than tonic activity levels do not factor into this result and were separately analyzed.

Recent work has implicated several subtypes of glypicans, astrocytic secreted proteins that promote glutamate receptor expression and induce functional synapse formation (Allen et al., 2012; de Wit et al., 2013). We previously showed that *GPC3*, a member of the glypican family, can drive increased peritumoral neo-synaptogenesis when expressed in GBM using our IUE CRISPR/Cas9 model (Yu et al., 2020). To further explore the role of other members of the glypican group during tumor progression in vivo, we generated gliomas with added GPC6 overexpression and followed these animals using the same experimental strategy as we used for the Cr86 tumors. Whereas Cr86 exhibited highly dynamic changes in tumor invasion patterns over time (Fig 3a), Cr86+GPC6 tumor dynamics remained within a significantly smaller range across all recorded time points (Fig 3b,c). This result was unexpected since like GPC3, GPC6 tumors were also expected to more aggressively promote peritumoral neosynapto-genesis. Further analysis will be needed to understand the disparate contributions of GPC homologs to tumorigenesis.

We applied the widefield image analysis processing pipeline introduced in Figure 4 to Cr86 and GPC6 recordings in order to explore whether different aspects of the calcium activity

that we are able to calculate, were significantly perturbed as a function of tumor invasiveness (in our case measured as growth rate), both when looking at the activity of the whole cortical window and also after binning the activity parameters in 0.75 mm-wide distance bands going outward from the tumor center. We found that overall, none of the metrics we analyzed in Cr86 animals – mean DF/F, calcium event amplitude, event area, and events/sec- showed a significant relationship between low (<10e5 μm^2/day) or high (>10e5 μm^2/day) tumor growth rates (Fig 5c (i)). This was true for GPC6 tumors as well, and is generally in agreement with the calcium baseline data from Figure 2. Note however, that this does not rule out slower, but nonetheless significant, changes over time that we did not scrutinize here as we exclusively related them with tumor growth rates which were derived from consecutive recordings. In contrast, when tumor growth rates were high, there was a significant elevation of calcium event amplitude near the tumor versus far, but only in Cr86 tumors (Fig 5 c (iii)). This indicates an unexpected but important difference in the way specific genetic makeup of GBM may influence the way it interacts with the surrounding microenvironment, and may lead to more precise diagnostics and treatments in the future.

The ability to analyze chronic changes in multiple aspects of cortical activity at these temporal and spatial scales underscores the power of this novel technique and is expected to be of significant value in studying a variety of rodent models of neurological disorders.

Acknowledgements

The authors wish to thank Ryan Ostrom for technical assistance. Supported by NCI R01CA223388 (JLN, BD) and Blue Bird Circle Foundation (JLN).

References

Alcoreza, O., Tewari, B. P., Bouslog, A., Savoia, A., Sontheimer, H., & Campbell, S. L. (2019). Sulfasalazine decreases mouse cortical hyperexcitability. *Epilepsia*, *60*(7), 1365–1377. https://doi.org/10.1111/epi.16073

Allen, N. J., Bennett, M. L., Foo, L. C., Wang, G. X., Chakraborty, C., Smith, S. J., & Barres, B. A. (2012). Astrocyte glypicans 4 and 6 promote formation of excitatory synapses via GluA1 AMPA receptors. *Nature*, *486*(7403), 410–414. https://doi.org/10.1038/nature11059

Buckingham, S. C., Campbell, S. L., Haas, B. R., Montana, V., Robel, S., Ogunrinu, T., & Sontheimer, H. (2011). Glutamate Release by Primary Brain Tumors Induces Epileptic Activity. *Nature Medicine*, *17*(10), 1269–1274. https://doi.org/10.1038/nm.2453

Campanella, R., Guarnaccia, L., Caroli, M., Zarino, B., Carrabba, G., La Verde, N., Gaudino, C., Rampini, A., Luzzi, S., Riboni, L., Locatelli, M., Navone, S. E., & Marfia, G. (2020). Personalized and translational approach for malignant brain tumors in the era of precision medicine: The strategic contribution of an experienced neurosurgery laboratory in a modern neurosurgery and neuro-oncology department. *Journal of the Neurological Sciences*, *417*, 117083. https://doi.org/10.1016/j.jns.2020.117083

Campbell, S. L., Robel, S., Cuddapah, V. A., Robert, S., Buckingham, S. C., Kahle, K. T., & Sontheimer, H. (2015). GABAergic disinhibition and impaired KCC2 cotransporter activity underlie tumor-associated epilepsy. *Glia*, *63*(1), 23–36. https://doi.org/10.1002/glia.22730

Cucchiara, F., Pasqualetti, F., Giorgi, F. S., Danesi, R., & Bocci, G. (2020). Epileptogenesis and oncogenesis: An antineoplastic role for antiepileptic drugs in brain tumours? *Pharmacological Research*, *156*, 104786. https://doi.org/10.1016/j.phrs.2020.104786

de Groot, J., & Sontheimer, H. (2011). Glutamate and the biology of gliomas. *Glia*, *59*(8), 1181–1189. https://doi.org/10.1002/glia.21113

de Wit, J., O'Sullivan, M. L., Savas, J. N., Condomitti, G., Caccese, M. C., Vennekens, K. M., Yates, J. R., & Ghosh, A. (2013). Unbiased Discovery of Glypican as a Receptor for LRRTM4 in Regulating Excitatory Synapse Development. *Neuron*, *79*(4), 696–711. https://doi.org/10.1016/j.neuron.2013.06.049

Eckert, M., Klumpp, L., & Huber, S. (2017). Cellular Effects of the Antiepileptic Drug Valproic Acid in Glioblastoma. *Cellular Physiology and Biochemistry*, *44*(4), 1591–1605. https://doi.org/10.1159/000485753

Gefroh-Grimes, H. A., & Gidal, B. E. (2016). Antiepileptic drugs in patients with malignant brain tumor: Beyond seizures and pharmacokinetics. *Acta Neurologica Scandinavica*, *133*(1), 4–16. https://doi.org/10.1111/ane.12437

Gill, B. J. A., Khan, F. A., Goldberg, A. R., Merricks, E. M., Wu, X., Sosunov, A. A., Sudhakar, T. D., Dovas, A., Lado, W., Michalak, A. J., Teoh, J. J., Liou, J. you, Frankel, W. N., McKhann, G. M., II, Canoll, P., & Schevon, C. A. (2022). Single unit analysis and wide-field imaging reveal alterations in excitatory and inhibitory neurons in glioma. *Brain*, awac168. https://doi.org/10.1093/brain/awac168

Hatcher, A., Yu, K., Meyer, J., Aiba, I., Deneen, B., & Noebels, J. (2020). Pathogenesis of Peritumoral Hyper-Excitability in an Immunocompetent CRISPR Based Glioblastoma Model. *Journal of Clinical Investigation*.

Jung, E., Alfonso, J., Osswald, M., Monyer, H., Wick, W., & Winkler, F. (2019). Emerging intersections between neuroscience and glioma biology. *Nature Neuroscience*, *22*(12), 1951–1960. https://doi.org/10.1038/s41593-019-0540-y

Keough, M. B., & Monje, M. (2022). Neural Signaling in Cancer. *Annual Review of Neuroscience*, *45*(1), null. https://doi.org/10.1146/annurev-neuro-111020-092702

Kerrigan, S., & Grant, R. (2011). Antiepileptic drugs for treating seizures in adults with brain tumours. *Cochrane Database of Systematic Reviews*, *8*. https://doi.org/10.1002/14651858.CD008586.pub2

Li, L., Zhang, C., Wang, Z., Guo, Y., Wang, Y., Fan, X., & Jiang, T. (2022). Expression changes in ion channel and immunity genes are associated with glioma-related epilepsy in patients with diffuse gliomas. *Journal of Cancer Research and Clinical Oncology*. https://doi.org/10.1007/s00432-022-04049-3

Lin, C.-C. J., Yu, K., Hatcher, A., Huang, T.-W., Lee, H. K., Carlson, J., Weston, M. C., Chen, F., Zhang, Y., Zhu, W., Mohila, C. A., Ahmed, N., Patel, A. J., Arenkiel, B. R., Noebels, J. L., Creighton, C. J., & Deneen, B. (2017). Identification of diverse astrocyte populations and their malignant analogs. *Nature Neuroscience*, *20*(3), 396–405. https://doi.org/10.1038/nn.4493

Montgomery, M. K., Kim, S. H., Dovas, A., Zhao, H. T., Goldberg, A. R., Xu, W., Yagielski, A. J., Cambareri, M. K., Patel, K. B., Mela, A., Humala, N., Thibodeaux, D. N., Shaik, M. A., Ma, Y., Grinband, J., Chow, D. S., Schevon, C., Canoll, P., & Hillman, E. M. C. (2020). Glioma-Induced Alterations in Neuronal Activity and Neurovascular Coupling during Disease Progression. *Cell Reports*, *31*(2), 107500. https://doi.org/10.1016/j.celrep.2020.03.064

Pace, A., Villani, V., Di Lorenzo, C., Guariglia, L., Maschio, M., Pompili, A., & Carapella, C. M. (2013). Epilepsy in the end-of-life phase in patients with high-grade gliomas. *Journal of Neuro-Oncology*, *111*(1), 83–86. https://doi.org/10.1007/s11060-012-0993-2

Piao, Y., Lu, L., & de Groot, J. (2009). AMPA receptors promote perivascular glioma invasion via β1 integrin–dependent adhesion to the extracellular matrix. *Neuro-Oncology*, *11*(3), 260–273. https://doi.org/10.1215/15228517-2008-094

Pnevmatikakis, E. A., & Giovannucci, A. (2017). NoRMCorre: An online algorithm for piecewise rigid motion correction of calcium imaging data. *Journal of Neuroscience Methods*, *291*, 83–94. https://doi.org/10.1016/j.jneumeth.2017.07.031

Podgorski, K., & Ranganathan, G. (2016). Brain heating induced by near-infrared lasers during multiphoton microscopy. *Journal of Neurophysiology*, *116*(3), 1012–1023. https://doi.org/10.1152/jn.00275.2016

Radin, D. P., & Tsirka, S. E. (2020). Interactions between Tumor Cells, Neurons, and Microglia in the Glioma Microenvironment. *International Journal of Molecular Sciences*, *21*(22), 8476. https://doi.org/10.3390/ijms21228476

Samudra, N., Zacharias, T., Plitt, A., Lega, B., & Pan, E. (2019). Seizures in glioma patients: An overview of incidence, etiology, and therapies. *Journal of the Neurological Sciences*, *404*, 80–85. https://doi.org/10.1016/j.jns.2019.07.026

Sørensen, M. F., Heimisdóttir, S. B., Sørensen, M. D., Mellegaard, C. S., Wohlleben, H., Kristensen, B. W., & Beier, C. P. (2018). High expression of cystine–glutamate antiporter xCT (SLC7A11) is an independent biomarker for epileptic seizures at diagnosis in glioma. *Journal of Neuro-Oncology*, *138*(1), 49–53. https://doi.org/10.1007/s11060-018-2785-9

Takano, T., Lin, J. H.-C., Arcuino, G., Gao, Q., Yang, J., & Nedergaard, M. (2001). Glutamate release promotes growth of malignant gliomas. *Nature Medicine*, *7*(9), 1010–1015. https://doi.org/10.1038/nm0901-1010

Tantillo, E., Vannini, E., Cerri, C., Spalletti, C., Colistra, A., Mazzanti, C. M., Costa, M., & Caleo, M. (2020). Differential roles of pyramidal and fast-spiking, GABAergic neurons in the control of glioma cell proliferation. *BioRxiv*, 2020.03.05.978825. https://doi.org/10.1101/2020.03.05.978825

Tewari, B. P., Chaunsali, L., Campbell, S. L., Patel, D. C., Goode, A. E., & Sontheimer, H. (2018). Perineuronal nets decrease membrane capacitance of peritumoral fast spiking interneurons in a model of epilepsy. *Nature Communications*, *9*(1), 4724. https://doi.org/10.1038/s41467-018-07113-0

Torres, D., & Canoll, P. (2019). Alterations in the Brain Microenvironment in Diffusely Infiltrating Low-Grade Glioma. *Neurosurgery Clinics of North America*, *30*(1), 27–34. https://doi.org/10.1016/j.nec.2018.08.001

Vecht, C. J., Kerkhof, M., & Duran-Pena, A. (2014). Seizure Prognosis in Brain Tumors: New Insights and Evidence-Based Management. *The Oncologist*, *19*(7), 751–759. https://doi.org/10.1634/theoncologist.2014-0060

Venkataramani, V., Tanev, D. I., Strahle, C., Studier-Fischer, A., Fankhauser, L., Kessler, T., Körber, C., Kardorff, M., Ratliff, M., Xie, R., Horstmann, H., Messer, M., Paik, S. P., Knabbe, J., Sahm, F., Kurz, F. T., Acikgöz, A. A., Herrmannsdörfer, F., Agarwal, A., … Kuner, T. (2019). Glutamatergic synaptic input to glioma cells drives brain tumour progression. *Nature*, *573*(7775), 532–538. https://doi.org/10.1038/s41586-019-1564-x

Venkataramani, V., Yang, Y., Schubert, M. C., Reyhan, E., Tetzlaff, S. K., Wißmann, N., Botz, M., Soyka, S. J., Beretta, C. A., Pramatarov, R. L., Fankhauser, L., Garofano, L., Freudenberg, A., Wagner, J., Tanev, D. I., Ratliff, M., Xie, R., Kessler, T., Hoffmann, D. C., … Winkler, F. (2022). Glioblastoma hijacks neuronal mechanisms for brain invasion. *Cell*, *185*(16), 2899-2917.e31. https://doi.org/10.1016/j.cell.2022.06.054

Venkatesh, H. S., Johung, T. B., Caretti, V., Noll, A., Tang, Y., Nagaraja, S., Gibson, E. M., Mount, C. W., Polepalli, J., Mitra, S. S., Woo, P. J., Malenka, R. C., Vogel, H., Bredel, M., Mallick, P., & Monje, M. (2015). Neuronal Activity Promotes Glioma Growth through Neuroligin-3 Secretion. *Cell*, *161*(4), 803–816. https://doi.org/10.1016/j.cell.2015.04.012

Venkatesh, H. S., Morishita, W., Geraghty, A. C., Silverbush, D., Gillespie, S. M., Arzt, M., Tam, L. T., Espenel, C., Ponnuswami, A., Ni, L., Woo, P. J., Taylor, K. R., Agarwal, A., Regev, A., Brang, D., Vogel, H., Hervey-Jumper, S., Bergles, D. E., Suvà, M. L., … Monje, M. (2019). Electrical and synaptic integration of glioma into neural circuits. *Nature*, *573*(7775), 539–545. https://doi.org/10.1038/s41586-019-1563-y

Ye, Z.-C., & Sontheimer, H. (1999). Glioma Cells Release Excitotoxic Concentrations of Glutamate1. *Cancer Research*, *59*(17), 4383–4391.

Yu, K., Lin, C.-C. J., Hatcher, A., Lozzi, B., Kong, K., Huang-Hobbs, E., Cheng, Y.-T., Beechar, V. B., Zhu, W., Zhang, Y., Chen, F., Mills, G. B., Mohila, C. A., Creighton, C. J., Noebels, J. L., Scott, K. L., & Deneen, B. (2020). PIK3CA variants selectively initiate brain hyperactivity during gliomagenesis. *Nature*, *578*(7793), 166–171. https://doi.org/10.1038/s41586-020-1952-2

Figure Legends

Figure 1: Integration of CRISPR/Cas9 engineered GBM model with multimodal recordings of cellular, widefield fluorescence and behavioral parameters enables comprehensive characterization of malignant invasion and impact on peritumoral neurons throughout tumor evolution.

A) Mouse embryo ventricles are injected and electroporated in utero at E16.5 with CRISPR-Cas9 sgRNA to excise Pten, Nf3 and Tp53 (and RFP, GFP or tagBFP to label malignant cells) in astrocytic lineages. At ~P32-35, AAV-GCaMP7f, AAV-jrGeco1a, AAV-FLEX–GCaMP8m + AAV-CamkIIa-0.4-Cre or AAV-FLEX-iGlusnfr + AAV-Ef1α-Cre or AAV-CamkIIa-0.4-Cre was injected intracortically in 6-8 overlapping locations ~1mm apart at 2 depths each (~300 µm, 600 µm). Thy1-GCaMP6S mice were not injected. After 2 weeks, a bilateral ~7x5 mm cranial window and 2-channel EEG (reference over cerebellum were placed.

B) Starting at ~P50, calcium or glutamate activity was recorded using an integrated microscope with instantaneously switchable 1-p and 2-p excitation light paths. 2-p fluorescence was acquired either in spiral (~12 Hz) or resonant scan (~30 Hz) configuration, 1-p widefield images at 100 Hz with an sCMOS camera. 2-ch EEG was simultaneously sampled at 10 kHz. Running wheel velocity was measured with a rotary encoder, pupil and eye movements were tracked with a dedicated IR camera, and whisking/frontal body movements were recorded with a second IR camera. An LCD monitor was used to display visual stimuli.

C) Examples of baseline (left) and seizure activity (right) from 2-p recordings: traces show (1) DeltaF/F calcium activity of ~200 simultaneously imaged neurons, (2) ipsilateral EEG voltage, (3) running velocity, (4) whisking, (5) eyelid position, (6) pupil diameter and gaze angle, (7) visual stimulus. Scale = 10 sec.

D) Long-term optical stability of cranial windows: widefield (top) and 2-p (bottom) images from the same animal at P62, P127, and P189. scale (top) = 1 mm, scale (bottom) = 0.1 mm

Figure 2: Abnormal glutamate accumulation outpaces spatial extent and temporal increase in baseline neuronal calcium activity in Cr86 tumor cortex.

A) Examples of dual-indicator widefield images (assembled post-hoc) : thy1-GCaMP6s mouse, calcium signal in magenta, tumor (tagBFP) shown in cyan. In contrast to the glutamate progression in B), the global baseline calcium signal does not significantly change as the tumor grows and invades.

B) Example of glutamate baseline fluorescence (orange) over time (tumor cyan), analogous to A): mouse injected with AAV-FLEX-iGlusnfr + AAV-Ef1α-Cre. Note steady increase in glutamate accumulation. Scale = 1 mm

C) Top: Black/white panels show calcium fluorescence of the widefield FOV in a Cr86 tumor cortex at 8 time points between P56 and P99; equal brightness scale in each image. Bottom: Colored panels show the rate of change in tumor fluorescence at weekly intervals, generated by dividing two B/W images from consecutive timepoints, normalizing by the number of days between those sessions and by the mean of the resulting image, applying a colormap (imageJ, “union jack”) and setting the scale limits to [0.5 1.5].

D) Analogous to A), B/W panels show the evolution of baseline glutamate fluorescence intensity in a different Cr86 tumor animal between P59 and P93 with equal brightness scaling. Note the distinct nonlinear, progressive changes in signal intensity not seen in the calcium reporter mouse (A). Colored panels were constructed and scaled as in A).

E) Left: To capture the dynamical changes in fluorescence between time points, we computed the CV (SD/mean), normalized by the number of days between recordings. These values from multiple recordings were binned in 10-day intervals for 8 calcium-reporter mice (blue) and 7 glutamate reporter mice (orange) and plotted over time. Right: Glutamate CV/day reached higher values than calcium (mean 0.09+/-0.02 sem vs, 0.04+/-0.0044 sem, p=0.008, Wilcoxon ranksum test). To account for potential sampling bias/undersampling, we extrapolated a 90th percentile datapoint for each animal instead of using the maximum value.

Figure 3: Tumor spatial fluorescence intensity over time reaches higher levels in Cr86 versus GPC6 tumor animals. Despite difference in tumor growth, mean survival of the two groups is not significantly different

A) Heterogeneous spatial evolution of Cr86 tumor fluorescence intensity changes between P59 and P132. Colored panels, generated from monochrome intensity images as in figure 2, show extensive invasion of the main tumor mass on the right hemisphere from P58 – P108 and moderate changes thereafter, whereas tumor cells on the left hemisphere are no longer visualized at the surface at an early stage, but invade more strongly at later time points.

B) Analogous example of tumor fluorescence evolution in a GPC6 tumor animal between P62 and P140. Note the lower intensity of tumor signal changes in this model vs the Cr86 model in A). Specifically, strong, localized growth was not sustained over long periods of time (e.g. P70/62 vs P76/70, white arrows), and overall fluorescence changes were on average lower than in the Cr86 example between all time points. At later stages, the tumor cell mass was no longer visible by surface imaging, although 2 photon imaging revealed tumor cells in deeper layers (see suppl. Figure).

C) Comparison of tumor images from 11 Cr86 and 8 GPC6 animals shows that Cr86 tumors invade the cortex in a more consistent and sustained manner than GPC6 tumors. Left: analogous to figure 2 c), we computed the CV (SD/mean), normalized by the number of days between recordings. These values from multiple recordings were binned in 10-day intervals for 11 Cr86 tumor mice (red) and 8 GPC6 tumor reporter mice (blue) and plotted over time. middle: Cr86 CV/day reached higher values than GPC6 (mean 0.065+/-0.011 sem vs 0.032+/-0.005 sem , p=0.032, Wilcoxon ranksum test). To account for potential sampling bias/undersampling, we extrapolated a 90th percentile datapoint for each animal instead of using the maximum value. Right: Kaplan-Meier survival curves for Cr86 and GPC6 animals show no significant differences despite the differences in tumor invasion.

Figure 4: Chronic calcium activity analysis at fast timescales and mesoscopic spatial scales enables analysis of the dynamical range of influence inside and beyond the tumor margin in Cr86 vs GPC6 tumor animals

A) 1-p widefield images are recorded at ~500x520 pixel resolution and 100Hz sampling rate. Images are downsampled temporally to 20Hz and spatially by a factor of 8, resulting in ~0.24mm pixel resolution. After computing active whisking and running periods, 300 sec of quiet wakeful activity is selected. For each pixel, a corresponding DF/F signal trace is computed, detrended, and thresholded at 3 SD above mean baseline noise level.

B) Using a snapshot image taken with a green/red filter (for RFP labeled tumor) or 400nm/blue filter (for BFP labeled tumor), the tumor margin is computed for each recording at different time points. This image is aligned and spatially downsampled as in (A), and pixels are assigned to distance bands of 0.75 mm width. Average DF/F traces are calculated for visualization, and pixels are binned into the respective 0.75 mm distance bands.

C) Each DF/F trace is processed to extract the following metrics: I) mean DF/F over the duration of each trace, ii) calcium transient event rate sec^{-1}), iii) mean event amplitude for each trace, iv) mean area under the curve of identified calcium events, and v) rhythmicity, i.e. the inverse of the width at half maximum amplitude for the distribution of inter-event intervals.

D) To visualize changes in activation patterns over time, values for the computed metrics are plotted pixel by pixel with the outline of the tumor overlaid in white. To determine a possible relationship between the distance to the tumor edge and the neuronal activity metrics, the linear fit R-square is computed. Next, distances to the tumor edge are scrambled via circular shuffling 500k times to create a bootstrapped null distribution and a p-value for the significance of the correlation.

E) Next, metric distributions for pixels binned into 0.75 mm-distance bands are computed, and compared, first across time for each distance bin, and then across distance for each time point (Kruskal-Wallis test with correction for multiple comparisons).

Figure 5: Neural activity pattern levels increase near the tumor edge when the tumor growth rate accelerates.

A) Example of pixel-wise calcium activity changes in a Cr86 tumor animal. From top to bottom, the colored panels show the 0.75 mm distance bands around the tumor mass, mean DF/F traces for these bands, mean DF/F, calcium events/sec, calcium event amplitude, calcium event area, and rhythmicity. White scale bar = 2 mm. Representative EEG traces from each time point are shown underneath. Horizontal scale = 60sec, vertical scale = 0.5 mV. We show 4 representative time points corresponding to increasing tumor coverage. At P42, no tumor cells were visible at the surface, so this time point serves as a control baseline. The tumor outline depicted here and used for further analysis is a simulation of the eventual tumor location at later time points. To the right hand side of the colored FOV panels are the mean FOV metrics across all recordings in this animal. Below the colored FOV panels we show the temporal evolution of linear regression significance values for the 5 metrics, computed using 500,000 shuffled bootstrap analysis iterations. Note the strong correlation between significant decrease in event amplitude and area with increasing tumor distance as the tumor growth rate begins to accelerate. For example, at P112, when the tumor growth rate exceeds 10e5 μm^2/day, the linear fit showing a strong decline in activity with distance from the tumor is highly significant ($p = 2*10e-6$).

B) Analogous to A), we show FOV metrics for a GPC6 tumor animal at 4 exemplary time points (P62, 89, 114, and 134). In contrast to the Cr86 animal, there is no significant relationship between tumor distance and calcium event amplitude ($p = 0.04$).

C) Comparison of Cr86 whole-FOV metric values (mean DF/F, calcium event amplitude, event area, events/sec) split up into recordings during which the tumor growth rate was either below or above 10e5 μm^2/day. i) For the 4 metrics shown here, there were no significant differences depending on the tumor growth rate (Wilcoxon ranksum test, p-values not shown). Data points were pooled from 33 recordings, 4 animals.
ii) Analogous to i), GPC6 tumor animals did not show any significant relationships between tumor growth rate and the 4 metrics shown here. Data pooled from 14 recordings, 2 animals. iii) Comparison of significance values obtained from the linear fits between tumor distance and calcium event amplitude, split up by high (>10e5) or low (<10e5) tumor growth rate. In Cr86 tumor animals, there was a significant difference between high and low tumor growth rate ($p=0.003$, Wilcoxon ranksum test, 32 recordings, 4 animals), whereas this was not the case for GPC6 animals (12 recordings, 2 animals). Note that for GPC6 animals, some values corresponding to negative tumor growth are not shown on the logarithmic scale.

Supplementary figure (supplement to figure 3)

Dual-color two-photon fluorescence of the same cortical FOV showing migrating GBM cells over 27 days. FOV from the cortical window with a GPC6 tumor shown in fig 3B. White scale bar = 100 μm. Top row: max projection of ~30-80 μm below the surface. Bottom row: max projection of ~500-580 μm below the surface. Cyan = tumor cells, magenta = calcium indicator

Figure 1: Integration of CRISPR/Cas9 engineered GBM model with multimodal recordings of cellular, widefield fluorescence and behavioral parameters enables comprehensive characterization of malignant invasion and impact on peritumoral neurons throughout tumor evolution.

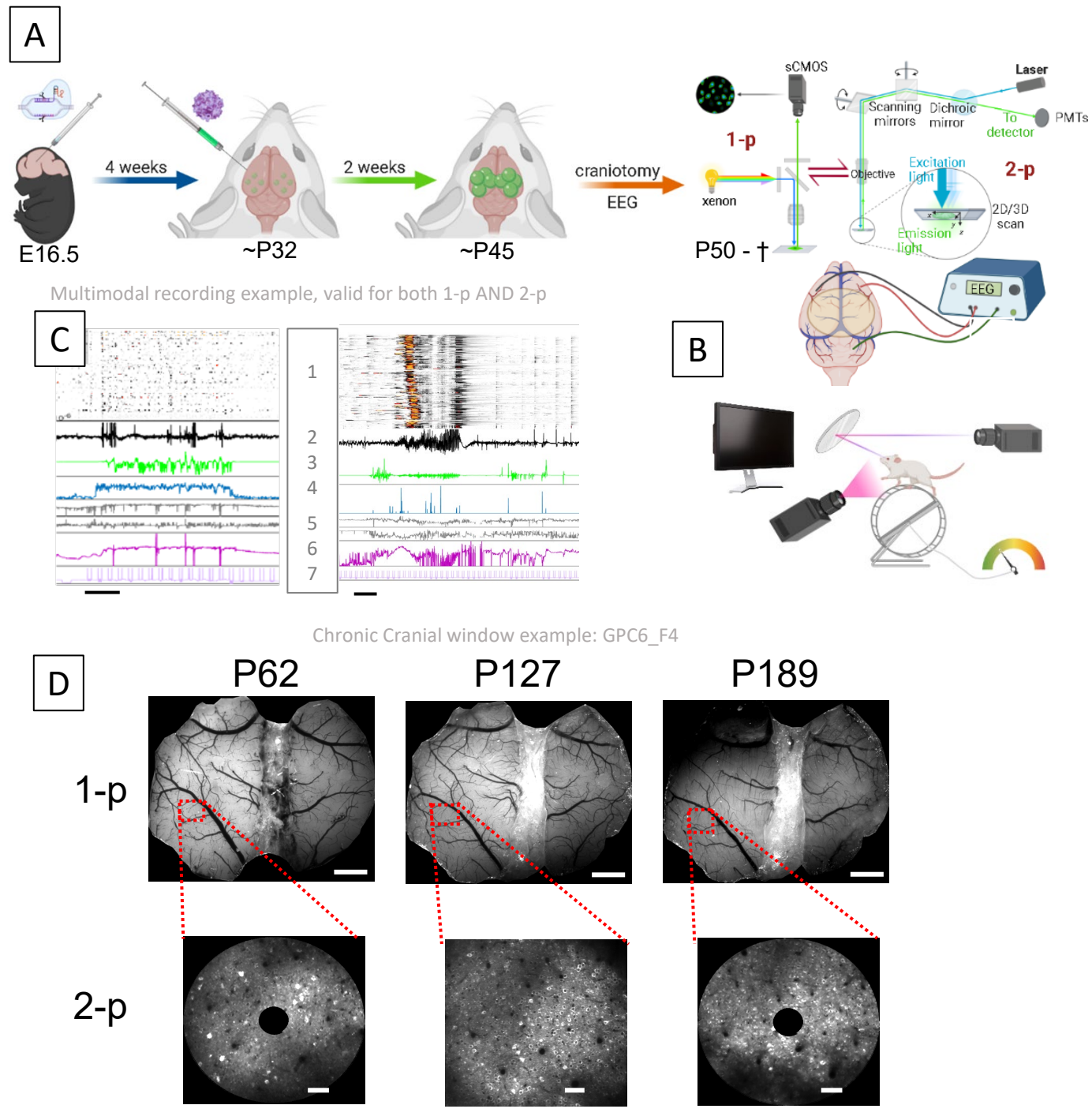

Figure 2: Abnormal glutamate accumulation outpaces spatial extent and temporal increase in baseline neuronal calcium activity in Cr86 tumor cortex.

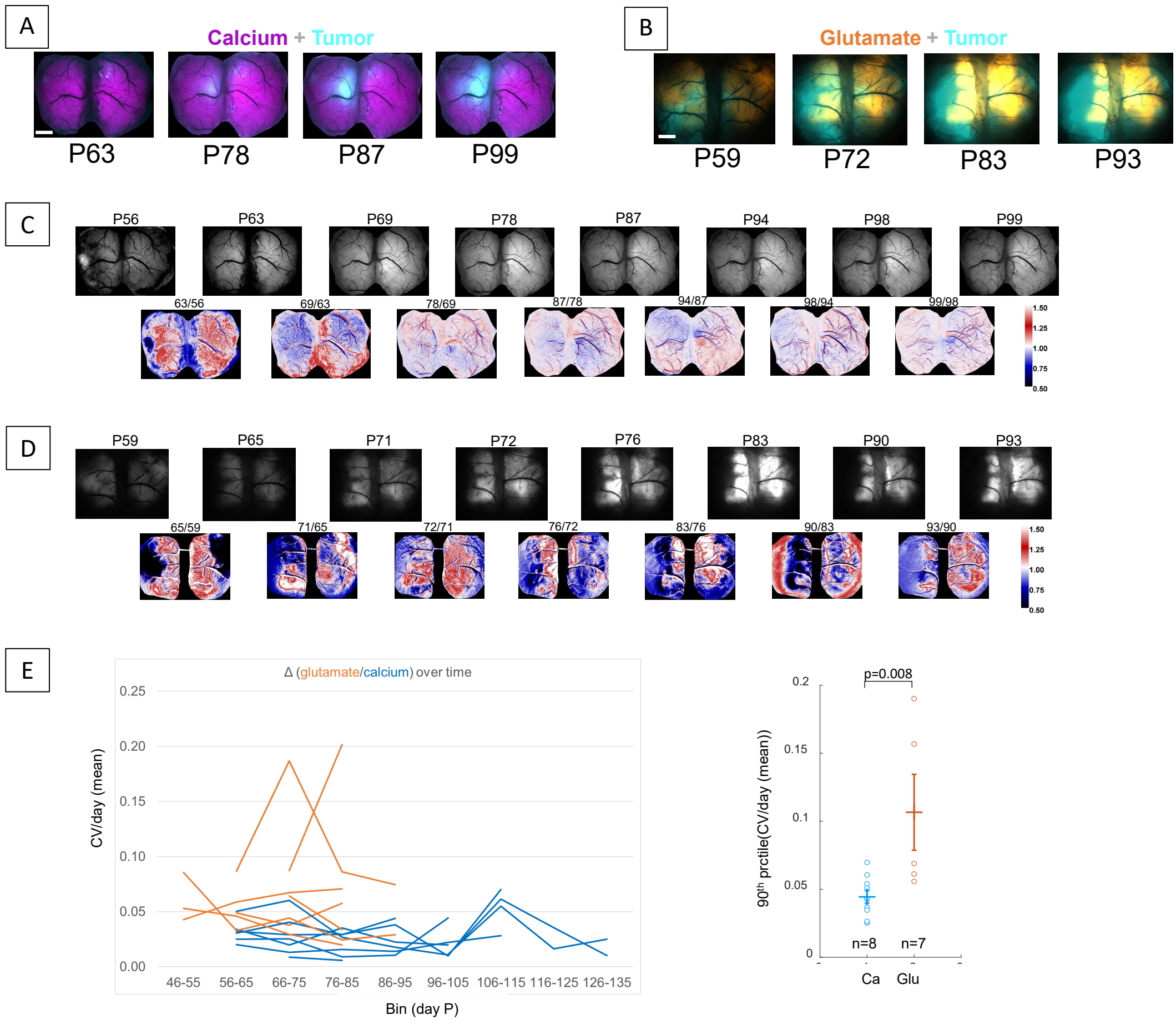

Figure 3: Tumor spatial fluorescence intensity over time reaches higher levels in Cr86 versus GPC6 tumor animals. Despite difference in tumor growth, mean survival of the two groups is not significantly different.

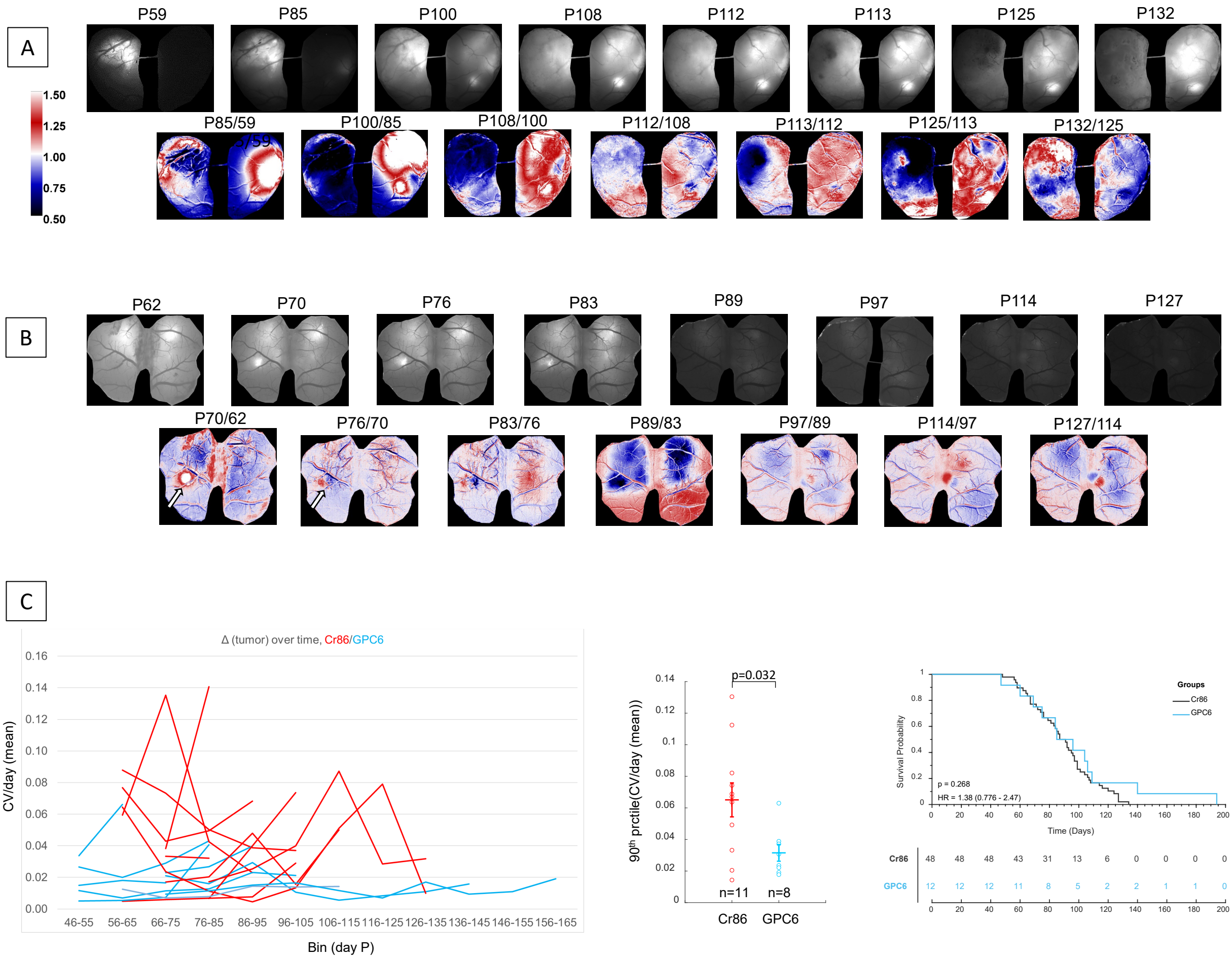

Figure 4: Chronic calcium activity analysis at fast timescales and mesoscopic spatial scales enables analysis of the dynamical range of influence inside and beyond the tumor margin in Cr86 vs GPC6 tumor animals

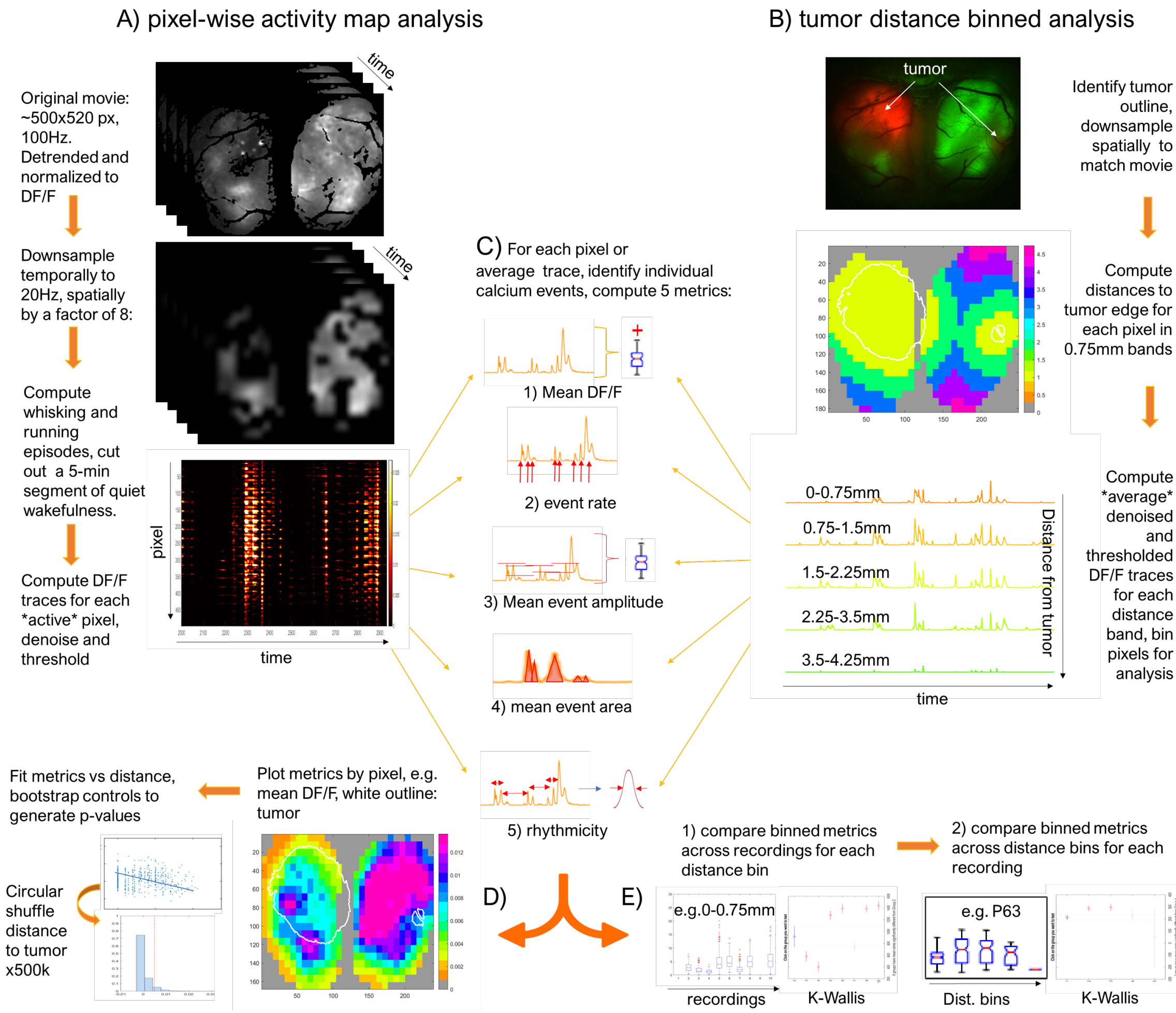
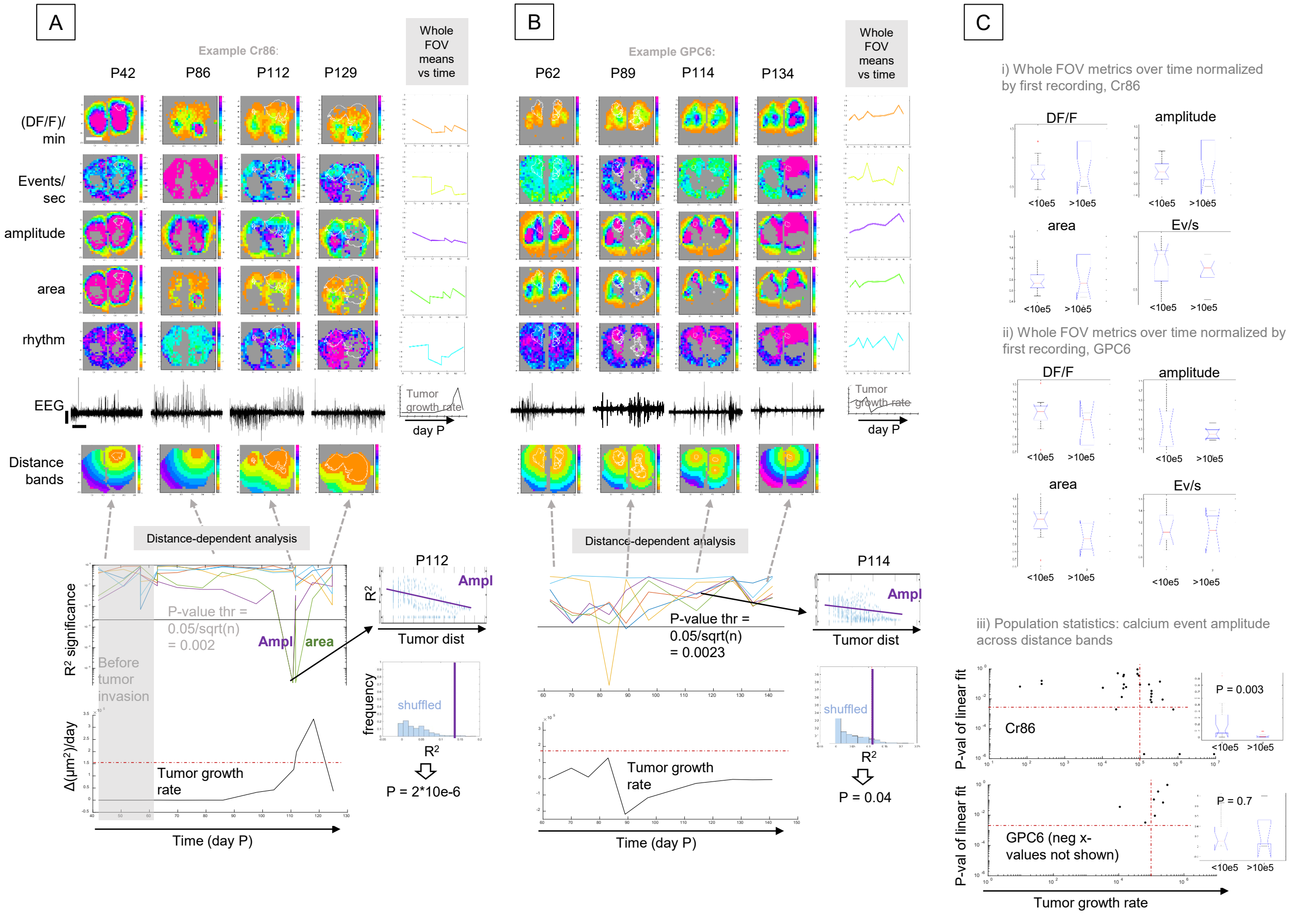
Figure 5: Neural activity pattern levels increase near the tumor edge when the tumor growth rate accelerates.